Available online at www.HEFJournal.org

ISSN: 2785-2997

Journal of
Human, Earth, and Future

Vol. 3, No. 1, March, 2022

Dispersion of Rayleigh Surface Waves and Electrical Resistivities Utilized to Invert Near Surface Structural Heterogeneities

Özcan Çakır [1*], Nart Coşkun [2]

[1] *Associate Professor, Department of Geophysics, Süleyman Demirel University, Isparta, Turkey*

[2] *Associate Professor, Department of Geophysics, Cumhuriyet University, Sivas, Turkey*

Received 29 December 2021; Revised 01 February 2022; Accepted 02 February 2022; Published 01 March 2022

Abstract

The single-station Rayleigh surface wave group velocities and electrical resistivities are two data sets that we cooperatively employ to image the near surface (< 40-m) anomaly structures. We numerically simulate the corresponding field measurements where the anomaly structures are assumed to have two-dimensional (2D) variations. The surface waves are represented by fundamental mode dispersion curves, and the electrical resistivities are assumed to be measured by using direct currents. We consider two types of anomaly structures, i.e., cavity and ore body. These two heterogeneities are easily distinguished from the surrounding geomaterial by their distinct physical properties. The cavity is characterized by low seismic velocity and high electrical resistivity, while the ore body is characterized by high seismic velocity and low electrical resistivity. The Rayleigh surface wave data is assumed to be collected throughout the classical common-shot gather. Multiple electrodes, multiple core cables, and multiple arrays are assumed to be used in the electrical survey. Both surface wave group velocities and electrical resistivities are shown to properly invert the anomalous structures in the subsurface. The surface wave group velocities have good horizontal resolution, while the corresponding vertical resolution is somewhat lower. The electrical resistivities have good resolution for shallow structures, but the resolution becomes somewhat reduced with increasing depth.

Keywords: Electrical Resistivity; Cavity; Group Velocity; Ore Body; Rayleigh Surface Waves.

1. Introduction

Geophysical inversion technologies have shown significant progress in delineating the physical properties (e.g., density, magnetic permeability, electrical conductivity, seismic velocity, attenuation, anisotropy) of the Earth's subsurface [1-9]. Consistent and comprehensive information about the subsurface is the most important goal to achieve in these geophysical inversions. The target depth can range from a few meters near the surface [10] to tens of kilometers in the crust and uppermost mantle system [11], and even thousands of kilometers on a global scale [12]. There are different methods that geophysical technology employs to explore the subsurface, i.e., electrical, gravity, magnetics, electromagnetics, and seismic. In these methods, the Earth is treated as a closed unknown system affected by some sort of energy (artificial or natural), which is dependent on the specific method applied, and then the Earth's response to the energy field is measured via some receivers deployed at different locations in the survey area. These receivers with response functions specific to the used method may be located on the free surface, in the downhole or at the ocean bottom. In some potential field applications (i.e., gravity and magnetics), airborne surveys are conducted using an aircraft flying at some altitude [13].

* Corresponding author: ozcancakir@sdu.edu.tr

http://dx.doi.org/10. 28991/HEF-2022-03-01-01

Numerous physical processes actively deform the Earth's structure, such as convections, rifting, subductions, collisions, isostasy, melting, magmatism, volcanism, earthquakes, subsidence, landslides, weathering, and erosion. These processes are largely driven by the movement of the lithospheric plates, i.e., plate tectonics. Some of these processes (e.g., subsidence, weathering) mostly deform the shallow subsurface while the other ones (e.g., subductions, collisions) are effective in the deep Earth structure with length scale reaching hundreds of kilometers. Therefore, the (unknown) Earth system, which may be considered either local (meters) or regional (kilometers), is truly three-dimensional (3D). There exist structural discontinuities in the horizontal and vertical directions. In the simplest case of one-dimensional (1D) multi-layered Earth media, the structural discontinuities occur mainly in the vertical direction [14]. In a fold-and-thrust belt (i.e., subduction and collision zones), the layer boundaries are folded and are displaced over some distances, creating discontinuities in the lateral direction, i.e., faults, nappes, and transitional slopes. In depositional environments, there may be clay and sand packets in the gravel background, creating 3D heterogeneities. Similarly, underground cavities (filled with air, water, soil, or rock), ore deposits, salt domes, sinkholes, partial melts, and fluids are some other 3D anomalies in the subsurface. To better understand the Earth's internal structure and composition, geophysical and geological data acquired by theoretical computations (modeling), laboratory tests (trials), and field surveys should be cooperatively utilized. Surface geological findings, geochemical studies, and information based on rock samples obtained from drill wells are combined with geophysical inversion efforts [15-17].

Different geophysical methods are sensitive to diverse physical properties of the subsurface [18]. For instance, the seismic method is primarily sensitive to underground velocity variations while the geoelectrical method is sensitive to electrical resistivity anomalies and the gravity method to density differences. The seismic method is essentially divided into four subsections, i.e., reflections, refractions, surface waves and receiver functions [19-24]. Joint inversions of seismic data obtained from applications of different seismic methods provide reliable information for the underground velocity structure. The seismic literature includes many such successful applications, e.g., joint inversion of reflections and surface waves [25], joint inversion of refractions and surface waves [5], joint inversion of P and S receiver functions [26], joint inversion of receiver functions and surface waves [27], joint inversion of Rayleigh and Love surface waves [28]. The seismic method is often combined with other geophysical methods, e.g., combined interpretation of reflections, refractions, surface waves and electrical resistivities [29], combined interpretation of refractions, surface waves and electrical resistivities [30], combined interpretation of seismic data (refraction and reflection) and potential fields (gravity and magnetics) [31], combined interpretation of electrical resistivities and surface waves [32]. There exist studies integrating various geophysical methods in one survey area, e.g., integrated analysis of gravity, magnetics, electrical resistivity, induced polarization, refraction, reflection, and ground penetrating radar [33].

Joint and cooperative analysis of the Earth's subsurface utilizing various geophysical methods gain support throughout the geosciences [34, 35]. We consider fundamental mode group velocity dispersion of Rayleigh surface waves and electrical resistivities to solve the underground structural heterogeneities. We assume that the observed Rayleigh surface waves are obtained from a traditional common-shot gather, i.e., pattern of single shot and linear geophone array. The group velocity dispersion curves are realized by the single-station analysis like the methodology (i.e., Multiple Filter Technique – MFT or Frequency–Time Analysis - FTAN) frequently employed in the earthquake seismology [11, 36, 37]. The single-station group velocity curve represents the average velocity structure between the source and receiver (geophone). Such group velocity curves attained at several geophone locations can be employed to solve the lateral velocity variation (two-dimensional – 2D) beneath the geophone array. The geoelectrical method considered in conjunction with the Rayleigh surface waves is based on examining the electrical conductivity anomalies developing from variations between rock units in the subsurface [38-42]. We follow a similar scheme to the surface waves for the electrical resistivity inversion. The apparent resistivity pseudo-section is computed based on a resistivity Earth model [14, 43], which is then inverted to estimate the underground (2D) resistivity-depth formation. Herein we are primarily interested in estimating the size and shape of near-surface buried objects (i.e., ore body and cavity) using Rayleigh surface waves and electrical resistivities in manner of cooperative inversion.

2. Materials and Methods

We consider one numerical model to test the performance of Rayleigh surface waves and electrical resistivities in delineating the 2D subsurface heterogeneities. The model structure is illustrated in Figure 1. In the background, the Earth structure is assumed to have a multi-layered formation and then this layered structure is assumed to be perturbed by 2D heterogeneities. In Figure 1 (upper panel), the shear-wave velocities (m/s) and electrical resistivities (Ω m) are shown. The other model parameters (both seismic and electrical) are listed in Table 1. The layer thickness (h), compressional-wave velocity (Vp), shear-wave velocity (Vs), density (d), shear-wave quality factor (Qs), compressional-wave quality factor (Qp) and electrical resistivity (ρ) are these model parameters utilized in the numerical calculations. As listed in Table 1, the electrical resistivity in the second layer is represented by two different values (i.e., 100 Ω m – low resistivity and 1000 Ω m – high resistivity), which are used to test the inversion effect of low and high resistivities above the considered anomaly structures.

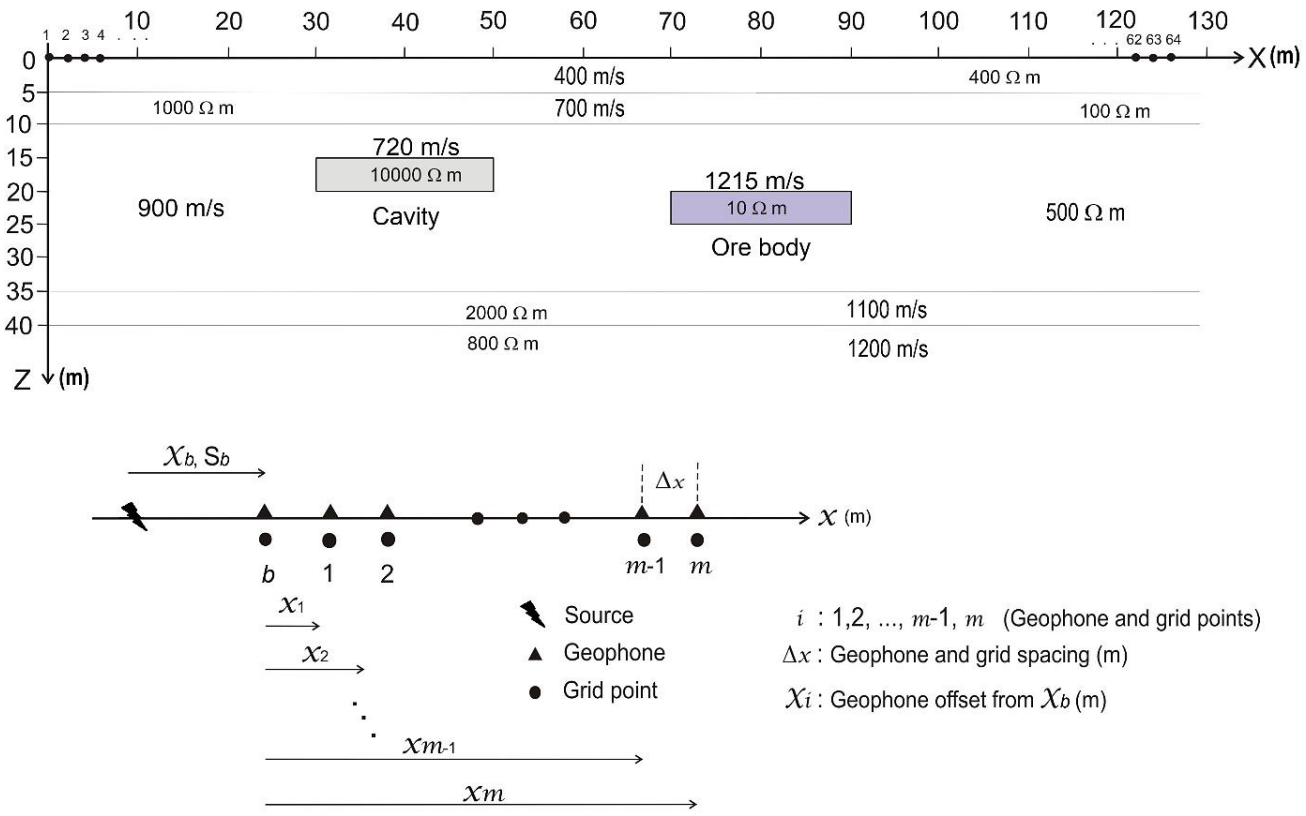

Figure 1. The multi-layered model structure in the near surface perturbed by 2D heterogeneities (cavity and ore body) are shown in the upper panel. The common-shot gather employed to collect Rayleigh surface wave data using vertical geophones is illustrated in the lower panel.

Table 1. The layer parameters for the multi-layered background model are listed. The compressional-wave quality factor is set to $Qp = 2Qs$

Layer number	h (m)	Vp (m/s)	Vs (m/s)	d (gr/cm^3)	Qs	ρ (Ω m)
1	5	700	400	1.6	50	400
2	5	1210	700	1.7	100	100-1000
3	25	1560	900	1.8	100	500
4	5	1900	1100	2.0	200	2000
5	∞	2100	1200	2.0	200	800

Figure 2 depicts the interaction between incident seismic surface waves and a buried cavity. The incident surface waves are Rayleigh type created by a seismic source located on the left. The cavity with a rectangular cross-section is assumed air filled. The incident Rayleigh surface waves are back-scattered (reflected and diffracted) by the cavity structure [44-48]. The reflected surface waves travel in the reverse direction towards the source, which are not shown in Figure 2 (section marked as *before*). The diffracted surface waves (see black arrows outside the anomaly in Figure 2) mostly created by sharp edges on the anomaly structure are more energetic [49-51]. Some of the incident surface wave energy is converted into body waves traveling as trapped air waves inside the cavity (see black arrows inside the anomaly in Figure 2). Most of the incident surface wave energy interacting with the cavity continue as accumulated on the border wall between the cavity and the surrounding geomaterial (see blue arrows in Figure 2). These focused surface waves around the upper boundary of the cavity couple to the surface waves directly traveling between the ground surface and the cavity. The other half of the incoming surface wave energy around the lower boundary of the cavity travel coupled to the surface waves below the cavity. The short wavelength (or high frequency) surface waves with relatively shallower depth penetration do not interact with the buried cavity. The total surface wavefield (i.e., leaving surface waves in Figure 2) on the right includes direct (incident) surface waves plus these surface waves modified by the presence of the cavity structure. The scattered energy off the cavity causes increased amplitudes in the section *above* the anomaly while the latter case causes decreased surface wave amplitudes in the section marked *after* in Figure 2 [52].

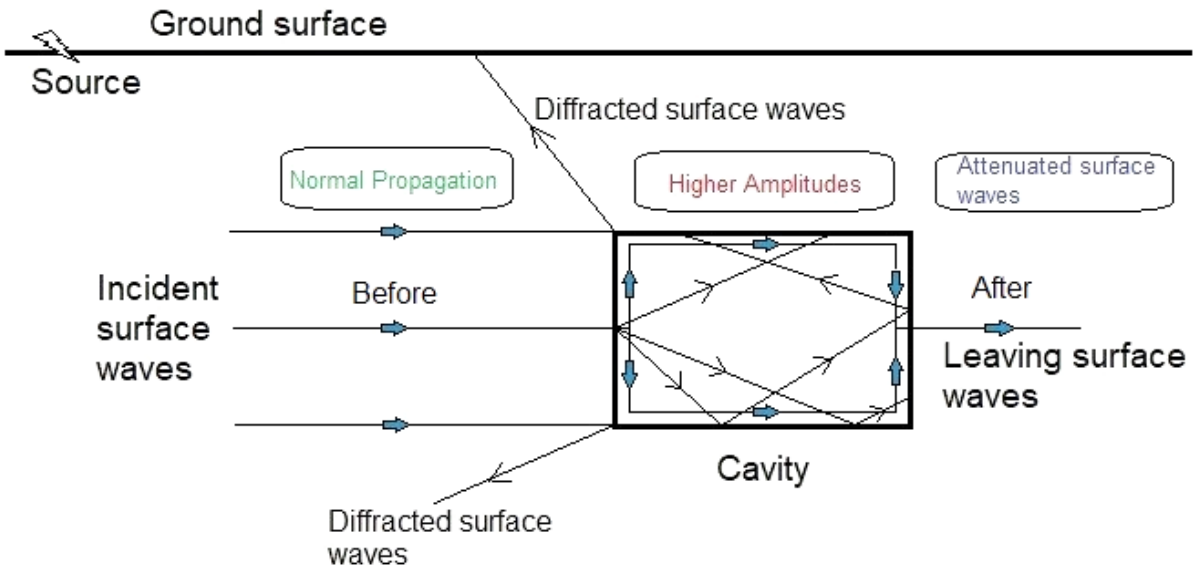

Figure 2. Surface waves propagating towards a buried cavity with rectangular cross-section are shown. Incident surface waves from the left (source), diffracted surface waves off the cavity, and surface waves propagating away from the cavity are illustrated [50, 52]. The cavity scatters the incoming surface waves and traps them inside as converted air waves. Seismic amplitudes on the receivers above the cavity are higher and surface waves leaving the cavity area are attenuated. Vertical and horizontal dimensions of the cavity are exaggerated for better visualization.

In Figure 1, the first heterogeneity with 20-m length at around 40-m distance represents a cavity in the depth range from 15-m to 20-m (i.e., thickness of 5-m). The second heterogeneity with again 20-m length at around 80-m distance stands for an ore body in the depth range from 20-m to 25-m (i.e., again thickness of 5-m). Both anomalous structures are assumed to have rectangular cross-sectional area. The cavity corresponds to the subsurface conditions with low velocity represented by *Vs*=720 m/s and high electrical resistivity represented by ρ=10000 Ω m in the respective depth range. The ore body is assumed to yield high velocity (i.e., *Vs*=1200 m/s) and low electrical resistivity (i.e., ρ=10 Ω m) conditions. In the depth range from 10-m to 35-m (i.e., background), the shear-wave velocity (*Vs*) is assumed to be 900 m/s while the electrical resistivity (ρ) is assumed to be 500 Ω m. The Rayleigh surface waves passing through the vicinity of the cavity are relatively slower [53]. We assume a low velocity depth section from 15-m to 20-m to replace the cavity structure, i.e., *Vs*=720 m/s, which is computed from 900*[20/(2.5+20+2.5)] m/s where the surface waves on the cavity wall are considered to travel extra 5-m. The other seismic parameters within the cavity are set to the following values, i.e., *Vp*=1200 m/s, *d*=1.20 gr/cm^3, *Qp*=10, *Qs*=5. Within the ore body the Rayleigh surface waves are relatively faster [47] for which we assume *Vs*=1215 m/s. For the ore body the other seismic parameters are assumed as follows, i.e., *Vp*=2100 m/s, *d*=2.10 gr/cm^3, *Qp*=9000, *Qs*=3000. Therefore, we model both anomalies as filled cavity where the first one is filled with low velocity material (-20% perturbation) and the second one with high velocity material (35% perturbation). In terms of the electrical resistivity, the filling material of the first cavity has ultra-high resistivity (10000 Ω m) while the second cavity is filled with ultra-low resistivity material (10 Ω m).

2.1. Surface Wave Method

We utilize the group velocity dispersion curves to invert the velocity structure beneath the geophone spread. The group velocity dispersion curves are obtained in a manner like the single-station approach commonly employed in the earthquake seismology. The travel time between the source (*x1*) and receiver (*x2*) can be expressed as follows [54].

$$t = \int_{x1}^{x2} \frac{1}{u(x)} dx = \int_{x1}^{x2} s(x) dx \tag{1}$$

where the distance range from *x1* to *x2* represents the travel path, *u(x)* is the group velocity, and *s(x)* stands for the group slowness. We employ a discretized version of Equation 1. The discretization is based on the data acquisition system (i.e., common-shot gather) illustrated in Figure 1 (lower panel). Equation 2 is the result of this discretization process.

$$\begin{bmatrix} 1&0&0&0&0&0&0&0&0&0&0 \\ 1&1&0&0&0&0&0&0&0&0&0 \\ 1&1&1&0&0&0&0&0&0&0&0 \\ & & & \vdots & & & & & & & \\ 1&1&1&1&1&1&1&1&1&1&0 \\ 1&1&1&1&1&1&1&1&1&1&1 \end{bmatrix} \begin{bmatrix} S_1 \\ S_2 \\ S_3 \\ \vdots \\ S_{m-1} \\ S_m \end{bmatrix} \Delta x = \begin{bmatrix} \bar{S}_1 - S_b \\ \bar{S}_2 - S_b \\ \bar{S}_3 - S_b \\ \vdots \\ \bar{S}_{m-1} - S_b \\ \bar{S}_m - S_b \end{bmatrix} x_b + \begin{bmatrix} \bar{S}_1 \\ 2\bar{S}_2 \\ 3\bar{S}_3 \\ \vdots \\ (m-1)\bar{S}_{m-1} \\ m\bar{S}_m \end{bmatrix} \Delta x \tag{2}$$

Here m describes the number of geophones and grid points. The group slowness computed from the single-station (observed) group velocity is given by $\bar{S}_i$ (known) and S_i (unknown) defines the group slowness at a grid point. S_b (Known) denotes the average group slowness corresponding to the pathway from the source to the base geophone indexed as b (see Figure 1 – lower panel). The base geophone could be selected as the first geophone or some other geophone in the array. The system in Equation 2 is solved for S_i at each surface wave period.

In real applications, the single-station (observed) group velocity curve can be obtained from the MFT (Multiple Filter Technique) analysis applied on the observed waveforms [14, 55]. Herein we do not apply the MFT, but rather simulate the observed slowness ($\bar{S}_i$) by forward solving the system in Equation 2. The $\bar{S}_i$ values are computed using the theoretical velocity-depth profile (S_i) below each grid point. For this computation the linear system in Equation 3 is utilized.

$$\begin{bmatrix} \bar{S}_1 \\ \bar{S}_2 \\ \bar{S}_3 \\ \vdots \\ \bar{S}_l \\ \bar{S}_m \end{bmatrix} = \begin{bmatrix} q_1 \\ q_2 \\ q_3 \\ \vdots \\ q_l \\ q_m \end{bmatrix} S_b x_b + \begin{bmatrix} q_1 & 0 & 0 & & 0 & 0 \\ q_2 & q_2 & 0 & \cdots & 0 & 0 \\ q_3 & q_3 & q_3 & & 0 & 0 \\ & \vdots & & \ddots & \vdots & \\ q_l & q_l & q_l & \cdots & q_l & 0 \\ q_m & q_m & q_m & & q_m & q_m \end{bmatrix} \begin{bmatrix} S_1 \\ S_2 \\ S_3 \\ \vdots \\ S_l \\ S_m \end{bmatrix} \Delta x \tag{3}$$

where $l = m - 1$ and $q_i = 1/(x_b + i\Delta x)$, $i = 1,2, \ldots, m-1, m$. Once the single-station group slowness values ($\bar{S}_i$) are computed from Equation 3, we employ Equation 2 to determine the group slowness values (S_i), which are then inverted for the velocity-depth profiles underneath grid points (Figure 1 – lower panel).

2.2. Geoelectrical Method

We utilize an open-source software by Blanchy et al. (2020) [56] to perform the Electrical Resistivity Tomography (ERT). This software (ResIPy along with graphical user interface – GUI and Python application programming interface – API) provides many utilities such as design of electrode spacing, triangular or quadrilateral mesh generation using certain shapes (i.e., flat layers, rectangles, and polygons), selection of electrode array, forward modeling, inversion parameter setting, data inversion, plotting and saving of inversion results. For the geoelectrical method we employ a linear electrode array with 64 electrodes and 2-m electrode spacing. The subsurface is digitized using a triangular meshing where flat layers and rectangular anomaly shapes are used. Figure 3 shows the corresponding numerical model, which is a digitized version of the analytical model introduced in Figure 1 (upper panel). In Figure 3, the triangular meshing gets coarser with depth since the sensitivity of geoelectrical data decreases with increasing depth. The color scale on the right indicates the resistivity values assigned for each subsurface depth section coded by different colors. The third color (i.e., light brown) in the color scale is labeled R, which represents two different resistivity values (i.e., 100 and 1000 Ω m) in the second layer from the top. The latter is in accordance with the case discussed in Figure 1 (upper panel). In Figure 3, there are 64 black dots indicating electrode positions on the ground surface.

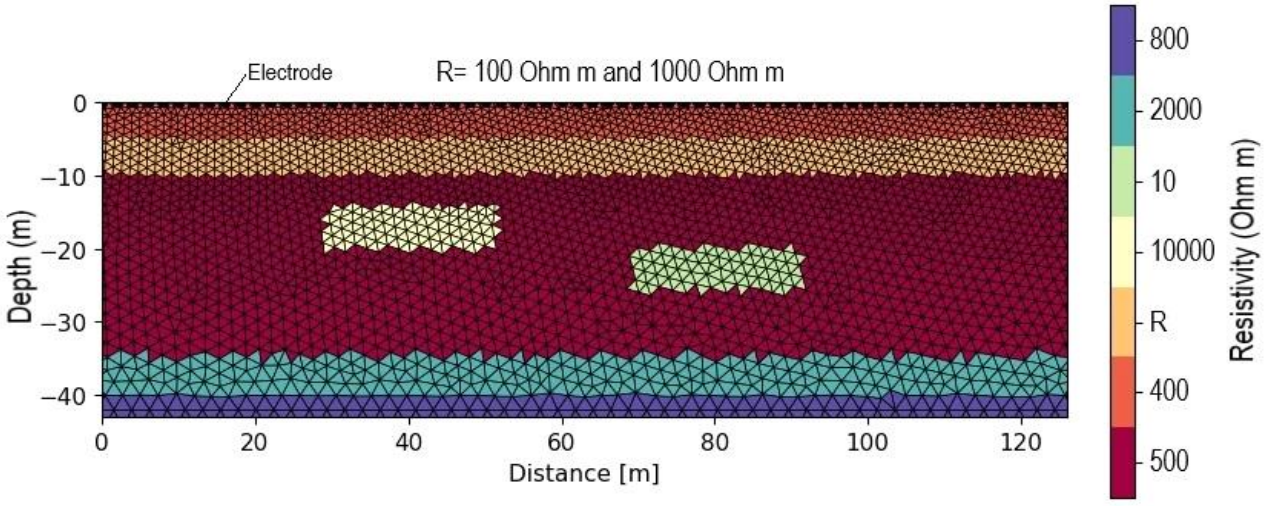

Figure 3. Numerical model along with triangular meshing used for geoelectrical inversion is shown.

The electrode arrays utilized in the electrical resistivity inversions are shown in Figure 4. All four electrode arrays are simultaneously utilized where the Dipole-Dipole array with a=2 and n=29 is represented by 870 quadrupoles in the apparent resistivity pseudo section. The number of quadrupoles for the Wenner array with a=21 is 651. The

Schlumberger array with a=2 and n=30 is represented by 870 quadrupoles. The Multi-Gradient array with a=2, n=62, and s=62 is represented by the highest number of quadrupoles, i.e., 18445.

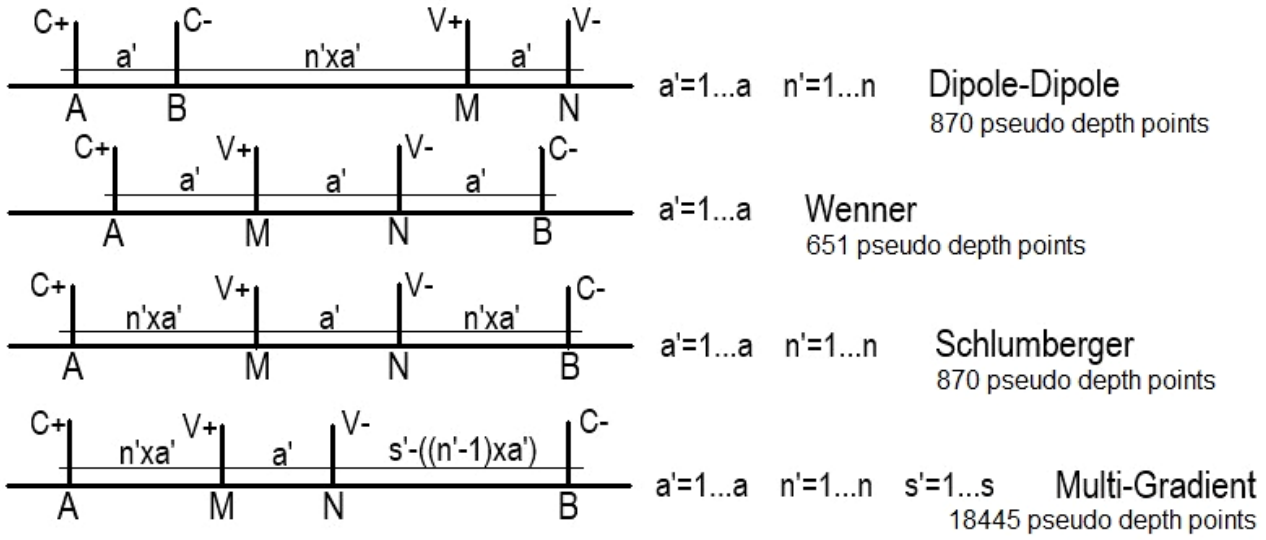

Figure 4. Electrode arrays used in the electrical resistivity tomography are shown. Electrical current is introduced into the subsurface using current electrodes A and B, and the voltage difference is measured via M and N potential electrodes. Geometrical relationship between current and potential electrodes are designed according to free parameters (a, n, s) shown alongside each array.

3. Numerical Results

Constructively interfering P (compressional waves) and SV (vertically polarized S waves) create Rayleigh surface waves. Constructive interference takes place between multiply reflected and refracted P and SV waves. There are also wave type conversions at the velocity discontinuities in the wave propagating media, i.e., from P-to-SV and SV-to-P. The Earth structure has a multilayered nature, which can be studied by the inversion of surface wave dispersion [57]. The Rayleigh surface waves impinging upon some heterogeneity in the Earth are scattered both in forward and backward directions. We simulate the forward scattering effect by considering low/high velocity zones in the subsurface (Figure 2), which leads us to obtaining approximate seismic images of the heterogeneous structures. In case of electrical resistivity, these heterogeneous subsurface structures with high resistivity repel the electrical currents away from the anomaly while these heterogeneous structures with low resistivity attract the electrical currents towards the anomaly. These two different electrical behaviors allow us to obtain approximate electrical image of the heterogeneous subsurface.

3.1. Surface Wave Inversion

The single-station group velocity dispersion curve is generally extracted from the observed surface waveforms by applying the multiple filter technique – MFT [55, 58]. As stated above, we follow a different method. The single station group velocities are theoretically computed from Equation 3 and then Equation 2 is used to convert these theoretical group velocities into group velocities at discrete points in the geophone array (see lower panel in Figure 1). We simulate the seismic noise conditions via the relation $u = \bar{u} + \sigma(r - 0.5)$ where u is noise-added group velocity (m/s), $\bar{u}$ is unperturbed group velocity (m/s) computed from Equation 2, r gives random number ($0 \leq r < 1$), and $\sigma = 30$ m/s describing the error bound. Some of the resulting group velocity dispersion curves (both single-station and discrete-point) at several distances (i.e., source-receiver distances given by 20-m, 40-m, 60-m, 80-m, and 100-m) are illustrated in Figure 5. The geophone array is designed as having 64 geophones with 2-m geophone spacing and 2-m offset to the first geophone. The system in Equation 2 is solved for the geophone sub-array from geophone #10 (20-m) to geophone #60 (120-m), which is our target area under which the velocity-depth inversion is considered. The base geophone is set to be geophone #9 with 18-m distance from the source. This 18-m distance may not be good enough to resolve deeper propagating (long wavelength) surface waves in which case the offset to the first geophone can be increased to, for instance, 10-m or longer by moving the source in the backward direction (to left in Figure 1, lower panel). The number of geophones can be increased to, for instance, 96 to cover these areas not covered by 64-geohpone array. The last two cases are a matter of field survey design.

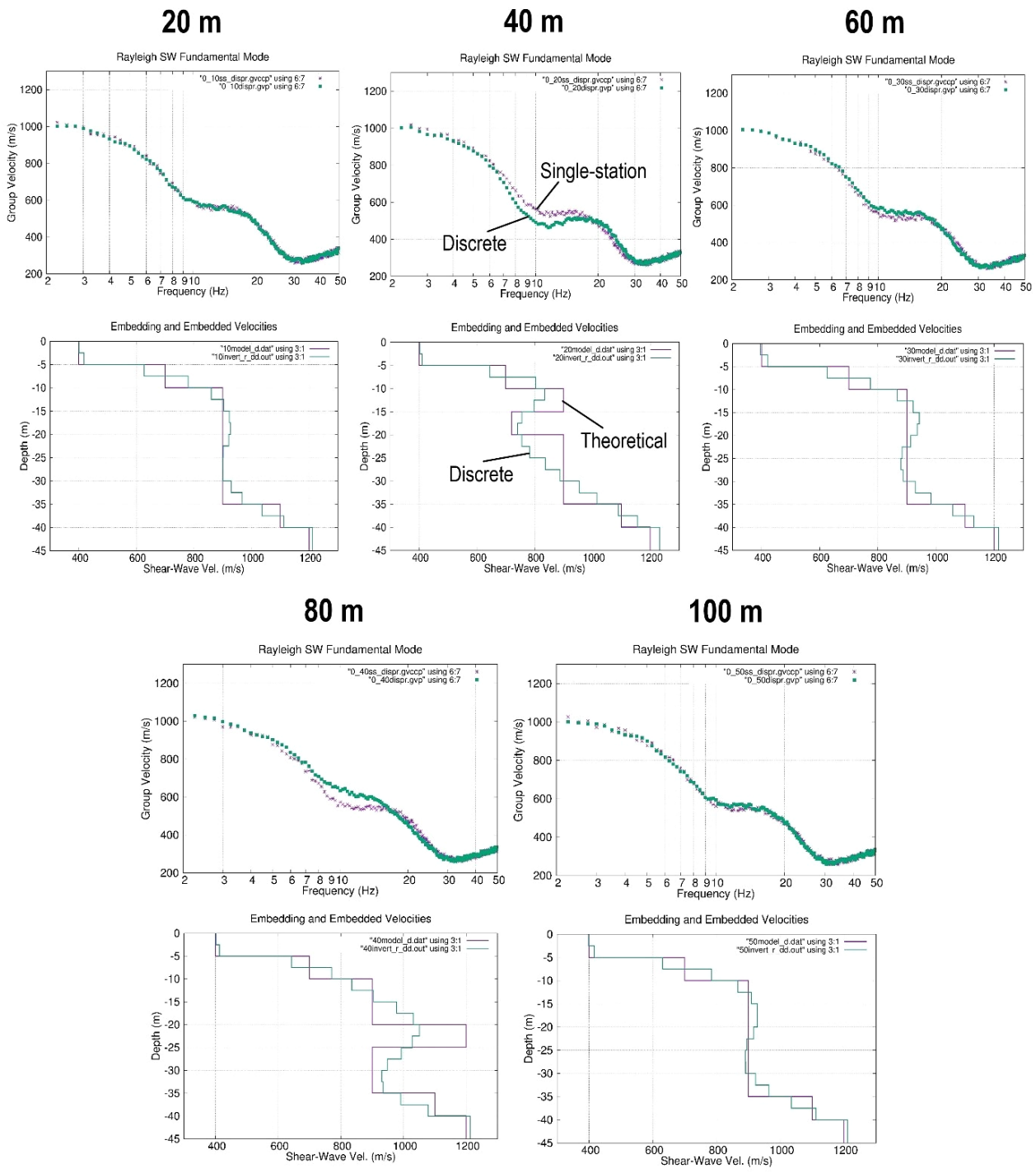

Figure 5. Dispersion curves (random noise added) and velocity-depth profiles at distances of 20-m, 40-m, 60-m, 80-m, and 100-m from the seismic source are shown. At each distance, dispersion curves are illustrated in the upper panel while velocity-depth profiles in the lower panel. Green color dispersion curve (marked single-station) represents the single-station group velocity curve obtained from Equation 3 and purple color dispersion curve (marked discrete) stands for the group velocity curve obtained from Equation 2. Purple color velocity-depth profile (marked theoretical) shows the theoretical model obtained from Figure 1 (upper panel) and green color velocity-depth profile (marked discrete) depicts the inverted velocity-depth profile.

In Figure 5 (upper panel at each distance point), the purple color dispersion curves represent the single-station group velocities at the corresponding source-station distance. The green color dispersion curves give the discrete-point group velocity curves, which are inverted for the velocity structure beneath the respective point. The differences between the single-station and discrete-point group velocity curves result from the perturbing effect of inhomogeneities (i.e., cavity and ore body) in the wave propagating media. The lower panel at each distance point in Figure 5 shows the two velocity-depth profiles where the purple color profile stands for the theoretical model while the green color profile shows the inverted model. The perturbed Earth structure involve sharp velocity discontinuities

along with low and high velocity zones. The surface wave group velocities can invert these anomalous depths. However, the resolution power is relatively lower since the corresponding surface waves with wavelength around 60 m, which is computed from 600-m/s phase velocity and 10-Hz frequency, is three times longer than the heterogeneity length (i.e., 20 m). Comparable wavelength to the heterogeneity size would result better resolution.

Figure 6 summarizes the group velocity inversion results in terms of 2D shear-wave velocity cross section where a rich color scale is used to show the velocity variations in detail. The model structure boundaries along with matching shear-wave velocities are displayed in Figure 6 where the two anomalous structures (cavity and ore body) are clearly visible throughout the color contrast with respect to the surrounding geomaterial. In general, the horizontal resolution is higher than the vertical resolution. The anomaly boundaries in the horizontal direction are better resolved than these boundaries present in the vertical direction. Both anomaly structures appear thicker than their actual size in the vertical direction (5-m). Note that on the 2D cross section particularly the deeper ore body is represented by lower seismic velocities (~1050 m/s) than the actual velocity at 1200 m/s. The latter is related to the lower resolution power of longer wavelength surface waves modeling the ore body (see Figure 5). The two flat layers near the surface (shallower than 10-m) are resolved well. The short wavelength (or high frequency) surface waves propagating near the surface are effective to achieve this higher resolution. There are also two other deeper velocity discontinuities at 35-m and 40-m depths. The velocity discontinuity at 35-m depth involves a velocity jump from 900 m/s to 1100 m/s while the other velocity discontinuity at 40-m depth is moderate involving a velocity jump of 100 m/s. The discontinuity at 35-m depth is resolved poorly and there exist some uncertainties at these depths below heterogeneity locations, i.e., it is upraised below the cavity and is depressed below the ore body. The discontinuity at 40-m depth is also resolved poorly. The depth confusion caused by the anomaly structures above is also evident for this depth range.

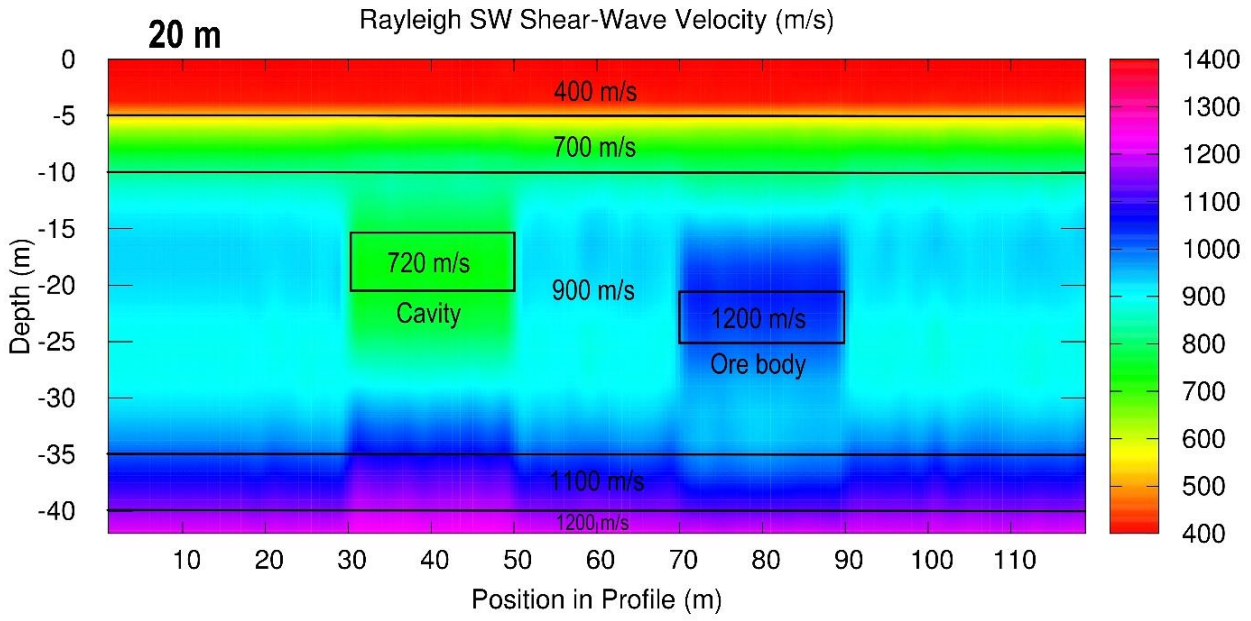

Figure 6. Shear-wave velocity cross section (2D) obtained from inversion of group velocity dispersion curves corresponding to the scheme outlined in Equations 2 and 3 is illustrated. Both heterogeneous structures (cavity and ore body) have 20-m length.

3.2. Electrical Resistivity Inversion

The theoretical model parameters for electrical resistivities in the subsurface are presented in Figure 1 and Table 1. For both forward and inverse electrical resistivity computations we utilize the software package provided by Blanchy et al. (2020) [56]. In the numerical resistivity computations, we simultaneously use four different multiple electrode arrays (i.e., Dipole-Dipole, Wenner, Schlumber, and Multi-Gradient) with 64 electrodes and 2-m electrode spacing, which gives 126-m profile length. The apparent resistivity values corresponding to the model structures are computed under random noise (3%) conditions. The true resistivity values are obtained by inverting the apparent resistivity pseudo-section. The inversion technique that we currently employ can resolve the heterogeneity structures and the layer thicknesses and resistivities particularly near the surface. We present the inverted resistivities in the form of 2D cross sections where the theoretical model parameters (anomalous structures and layer interfaces) are superimposed on each cross section. The change of the inverted resistivities with depth are depicted using a rainbow color scale.

Figure 7 shows the apparent resistivity pseudo section obtained after forward modeling of the model structure with the resistivity value of 100 Ω m in the second layer from top (see Figure 1, upper panel). In the pseudo cross section, the resistivity-depth distribution is represented by 20836 pseudo depth points where the number of pseudo depth

points contributed by each electrode array is given in Figure 4. The Multi-Gradient array is represented by the highest number of pseudo depth points. The inverted resistivity values corresponding to the resistivity data in Figure 7 are illustrated in terms of a 2D cross section in Figure 8. The two anomaly structures at 40-m and 80-m distances are clearly visible on the inverted cross section. The high resistivity anomaly on the left is depicted by the tones of red color and the low resistivity anomaly on the right by the tones of blue color. However, the rectangle shape of each anomaly is poorly imaged on the inverted cross section where the sharp edges are not recovered well by the inverted resistivities, and the anomaly structures are inverted deeper than their actual depths. The depth error is ~2 m for the shallower anomaly while it is ~4 m for the deeper anomaly. As indicated by an arrow, there appears a false high resistivity (~1200 Ω m) packet to the right on the cross section. In addition, the depth section to the left around the high resistivity anomaly is inverted with resistivities higher (~1200 Ω m) than the model structure (500 Ω m). Although there is some roughness in each layer, the resistivity-depth distribution indicates clear evidence for the occurrence of two horizontal layers in the near surface. Our theoretical model includes two other horizontal layers placed below the anomalous structures (see Figures 1 and 3 and Table 1) where the deeper layer represents the half-space. The resistivity cross section in Figure 8 does not show any sign of these two deep layers since the electrical currents do not properly reach this depth range.

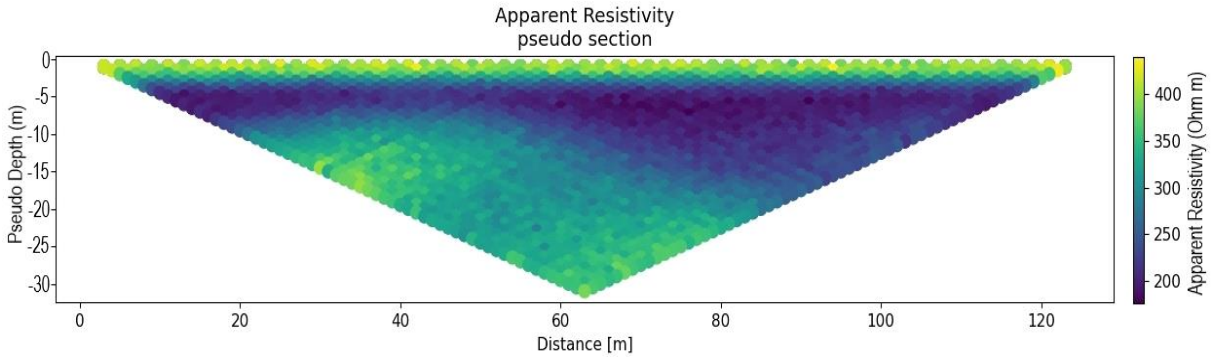

Figure 7. The resistivity cross section (2D) relating to the model structure (Figure 1 upper panel and Table 1) is shown in terms of the apparent (observed) resistivity values. Electrical resistivity in the second layer is 100 Ω m.

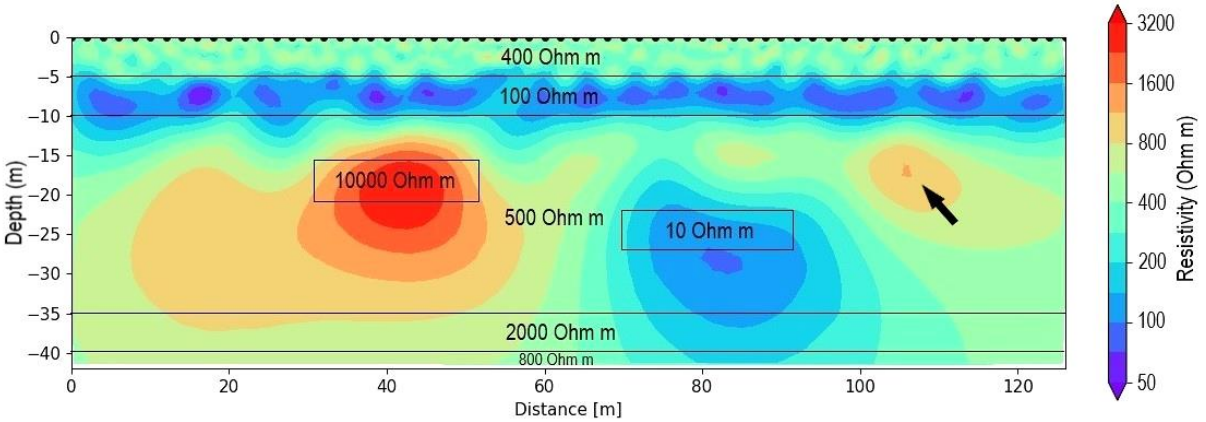

Figure 8. The resistivity cross section (2D) relating to the model structure (Figure 1 upper panel and Table 1) is shown in terms of the true (inverted) resistivity values. Electrical resistivity in the second layer is 100 Ω m.

For the next resistivity modeling we increase the resistivity value in the second layer 10 times (i.e., 1000 Ω m). The resulting apparent resistivity pseudo section obtained after forward modeling of the model structure is shown in Figure 9. The same number of pseudo depth points (i.e., 20836) along with the same set of electrode arrays (i.e., Dipole-Dipole, Wenner, Schlumberger, and Multi-Gradient) are also employed for this numerical test. Note that the apparent resistivity pseudo section in Figure 9 is quite different than that in Figure 7. The pseudo section in Figure 9 indicates better the locations of the anomaly structures, which is the result of the resistivity difference in the second layer. Figure 10 shows the resulting 2D resistivity cross section obtained after the resistivity inversion. The inverted cross section clearly shows the two anomaly structures, i.e., high resistivity anomaly portrayed in red color at 40-m distance and low resistivity anomaly portrayed in blue color at 80-m distance. In a similar manner to Figure 8, the inverted cross section poorly resolves the actual rectangle shape of anomaly structures. The sharp edges appear smoothed out. However, depths to the anomaly structures are determined better in this example. Both anomalies appear a little deeper than their actual positions. To the left and right there appear some false high resistivity (~900 Ω m) depth sections on the cross section. The latter is a result of poor data coverage in the resistivity measurements (see Figure 9), which is

also the case with the former example (see Figures 7 and 8). In this example, the roughness revealed by the inverted resistivities in the first two layers from top is higher compared to the former example, but the cross section still serves some evidence for the existence of two horizontal layers in the near surface. The two deep layers (i.e., one layer over half-space – see Figures 1 and 3 and Table 1) is again not resolved in the resistivity cross section (compare Figure 8 and 10). Since the electrical currents do not penetrate depths below ~30 m, these two deep layers are not properly inverted. Increased profile length (for instance 200-m) along with increased number of electrodes (for instance 128) may help resolve layers as deep as 50 m.

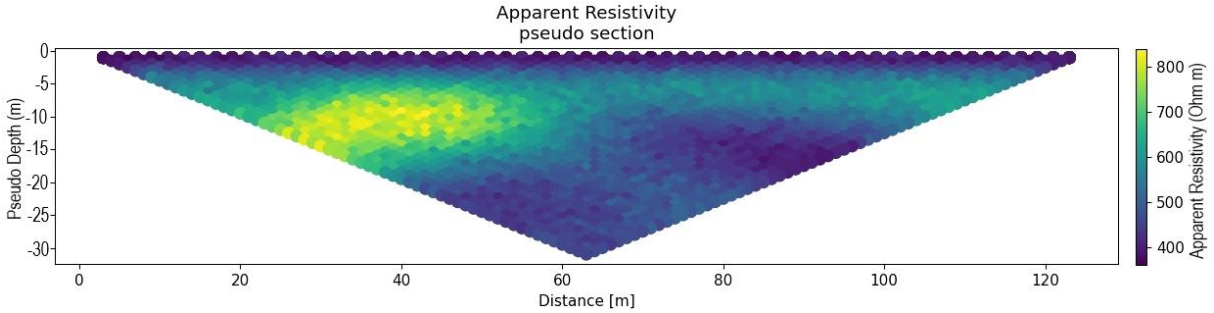

Figure 9. The resistivity cross section (2D) relating to the model structure (Figure 1 upper panel and Table 1) is shown in terms of the apparent (observed) resistivity values. Electrical resistivity in the second layer is 1000 Ω m.

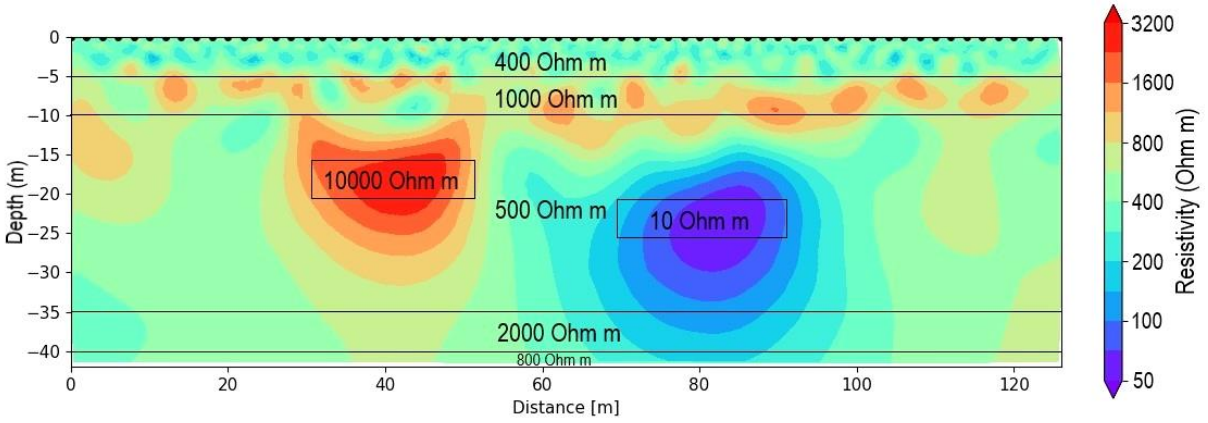

Figure 10. The resistivity cross section (2D) relating to the model structure (Figure 1 upper panel and Table 1) is shown in terms of the true (inverted) resistivity values. Electrical resistivity in the second layer is 1000 Ω m.

4. Discussions and Conclusion

The two modern geophysical methods, i.e., Rayleigh surface waves and electrical resistivities are frequently used in determining the physical properties of the subsurface structure. In the current study, we examine how effectively these two methods work together. The real earth shows low frequency (e.g., flat-lying layers) plus high frequency (e.g., inclusions such cavity, ore body, melt, sink hole, fluid, salt) structural features. Herein, we primarily focus on inclusions (i.e., cavity and ore body). These heterogeneities with variations in two-dimensional (2D) space are assumed embedded in the layered Earth (see Figure 1, upper panel). The Rayleigh surface waves are represented by fundamental mode dispersion curves while the electrical resistivities are assumed to be measured by direct currents. Both surface wave and electrical resistivity measurements are numerically simulated along with forward and inverse solutions.

We model both cavity and ore body as filled cavity. If the cavity is air-filled, then the corresponding seismic velocity is very low, i.e., seismic waves do not propagate effectively inside the cavity and the corresponding electrical resistivity is very high, i.e., electrical currents do not flow effectively inside the cavity. We approximate the very low seismic velocity of the air-filled cavity with a low seismic velocity. In a similar manner, we approximate the very high electrical resistivity of the air-filled cavity with a high electrical resistivity. We then apply the classical normal mode theory to compute the group velocity dispersion curves [59, 60]. The mathematical theory employed by Blanchy et al. (2020) [56] in the software package of ResIPy works effectively with high resistivity models. These two approximations for the seismic velocities and electrical resistivities are reasonable to represent the cavity in the subsurface. The case of the ore body is different than the cavity. The cavity is again filled, but this time with a high velocity and low resistivity geomaterial, i.e., inside the ore body the surface waves are fast, and the electrical currents flow easily. Both normal mode theory and ResIPy work effectively to model the physical properties inside the ore body.

In Figure 11, we consider two more models to represent the cavity and ore body structures in the subsurface. In the first model (upper panel), both heterogeneities are represented by 15-m length while in the second model (lower panel), the length is decreased to 10-m. The cavity structure in the first model is represented by a shear-wave velocity at 675 m/s, i.e., 900*[15/(2.5+15+2.5)] m/s. The shear-wave velocity in the second model is set to 600 m/s; i.e. 900*[10/(2.5+10+2.5)] m/s. In both models, the shear-wave velocity in the ore body structure is kept unchanged at 1200 m/s. Both cavity and ore body are also kept at the same thickness, i.e., 5-m. In general, to detect a subsurface anomaly is more difficult when the anomaly size becomes smaller, and the anomaly depth increases. In Figure 11, we try to show that the surface wave group velocities are still effective to detect these anomalous structures even if the anomaly sizes are considerably decreased. The resolution performance illustrated in Figure 11 imply that these anomalous structures even with 5-m length can be resolved in the surface wave group velocity inversion. We should mention that we currently consider only moderate noise conditions described above. In real applications, severe noisy conditions may prevail in which case smaller and deeper anomalies may not be properly resolved.

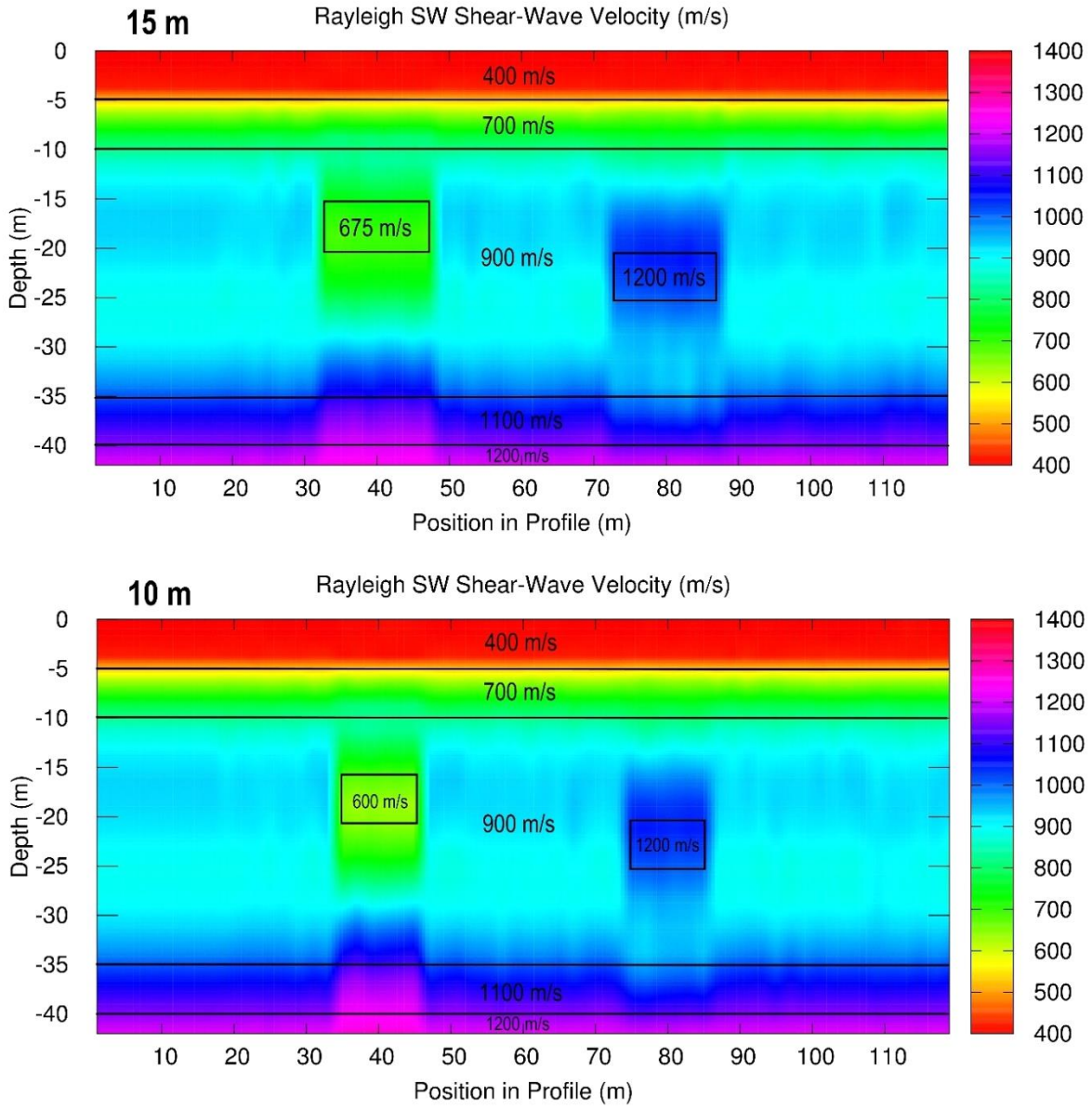

Figure 11. Shear-wave velocity cross sections (2D) obtained from inversion of group velocity dispersion curves corresponding to the scheme outlined in Equations 2 and 3 are illustrated. Upper panel: both heterogeneous structures (cavity and ore body) have 15-m length and lower panel: 10-m length.

We extend the inversion test outlined in Figure 11 to the electrical resistivities. The high (10000 W m) and low (10 W m) electrical resistivity values considered for the cavity and ore body, respectively, as well as thickness (5 m), are kept unchanged, but the corresponding anomaly length is decreased in the same way as shown in Figure 11. However, for the case of electrical resistivity, we examine only one length reduction, i.e., the anomaly length is decreased from 20-m (see Figures 7 to 10) to 12-m. The new results for the electrical resistivity inversions are illustrated in Figure 12,

where we use two panels to present the results. These two panels differ according to the resistivity value assigned to the second layer from the top (see Figure 1). The upper panel displays the inversion results obtained with 100 W m and the lower panel with 1000 W m. The upper panel in Figure 12 shows that despite the decreased length, the two anomalous structures are still distinguishable on the resistivity cross section. However, there is a possibility that these two higher resistivity packets indicated by the white arrows may be mistakenly interpreted as some real anomaly. The lower panel in Figure 12 reflects a somewhat different resistivity cross section than the one in the upper panel, which is the result of increased resistivity in the second layer, i.e., 100 W m versus 1000 W m. In the lower panel, the two anomalous structures are better isolated (i.e., color contrast) from the surrounding geomaterial, although the depth extent shows some uncertainty. As the two black arrows indicate, there exist two low resistivity packets that may be mistaken as real anomalies. In each panel, the near surface resistivity-depth distributions evidence the two-layer structure. To better model the electrical resistivities in Figure 12 and those in Figures 8 and 10, one needs to create finer meshing in the subsurface than presently utilized (see Figure 3). The latter requires higher memory (RAM) and more processing (CPU) capacity than we currently have. Therefore, we were not able to pursue the calculations in Figure 12 further.

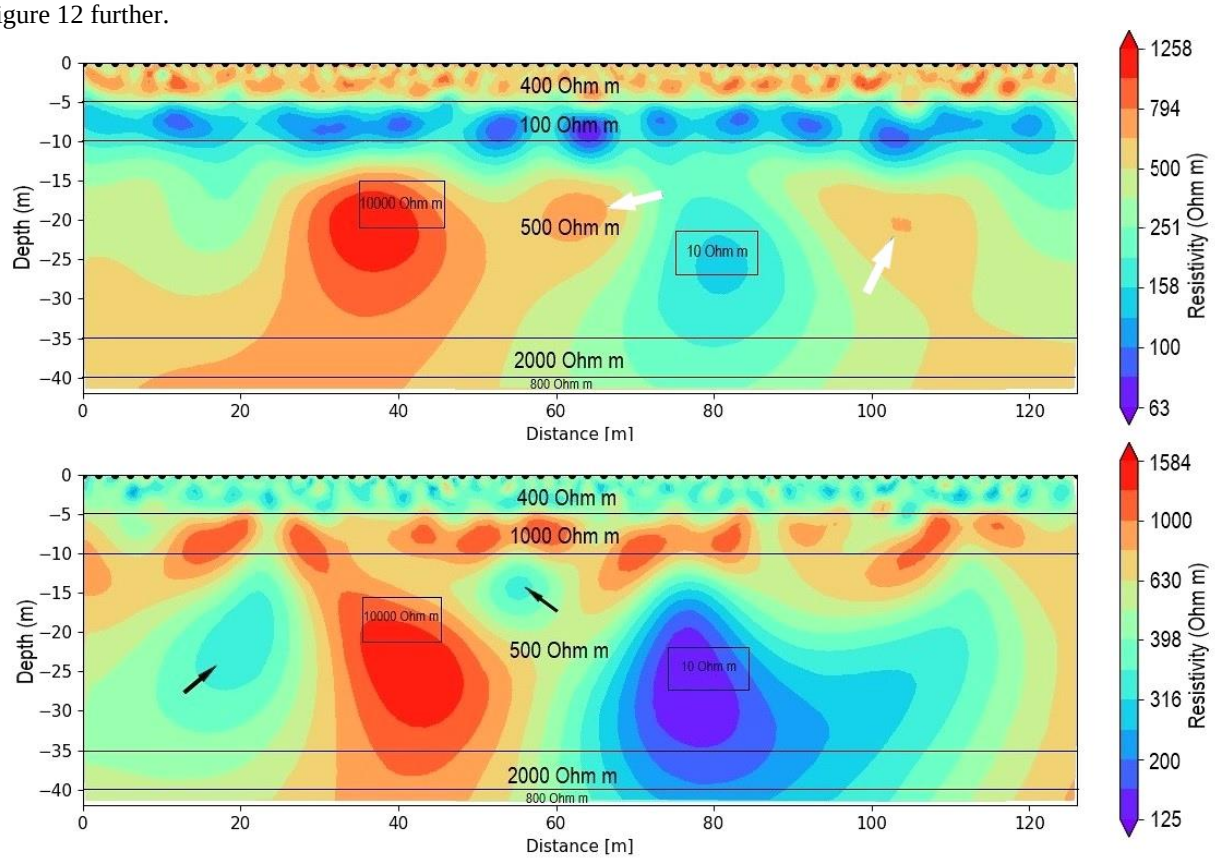

Figure 12. The resistivity cross sections (2D) are shown in terms of the true (inverted) resistivity values. The anomaly (rectangular shapes) length is decreased to 12-m. Electrical resistivity in the second layer is 100 Ω m (upper panel), and 1000 Ω m (lower panel).

Table 2 lists some lithologies along with the pertinent seismic velocities and electrical resistivities where the mentioned classifications (high or low) are relative to the surrounding geomaterial. The cases relevant to the air-filled cavity and ore body are discussed above. A hard rock environment in the subsurface would mean high seismic velocity and high electrical resistivity. On the other hand, a sand and clay packet in the subsurface would mean low seismic velocity and high electrical resistivity. These different combinations of high and low seismic velocities and electrical resistivities are effective for identifying the physical characteristics of the subsurface anomaly structures. The current study shows that the Rayleigh surface wave method and the electrical resistivity method can be used together to tell the difference between the different lithologies in Table 2.

Table 2. Different subsurface heterogeneity structures and the corresponding relative seismic velocities and electrical resistivities [61-64]

Lithology	Seismic velocity	Electrical resistivity
Hard rock environment	High	High
Sand and clay packet	Low	Low
Air-filled cavity	Low	High
Ore body	High	Low

Herein we emphasize the importance of multiple geophysical methods employed in an integrated manner in solving inversion problems of a survey area. Different geophysical methods (e.g., electromagnetics, magnetics, gravity, seismic, and electrical) show sensitivity to different physical properties (i.e., density, permeability, conductivity, velocity, porosity, anisotropy, attenuation, and resistivity) in the Earth. In this respect, one geophysical method may somewhat fail to locate the target anomaly at the correct size and depth. Another geophysical method with better horizontal and vertical resolution power may help to clarify such ambiguities. Disturbing field conditions (e.g., weather, noise, electrical wiring, humidity, paving, and infrastructure) may render a preferred geophysical method unsuccessful. Hence, various geophysical methods that are cooperatively employed should be more beneficial than if these methods are applied on their own.

5. Declarations

5.1. Author Contributions

Conceptualization, Ö.Ç. and N.C.; methodology, Ö.Ç. and N.C.; software, Ö.Ç. and N.C.; validation, Ö.Ç. and N.C.; formal analysis, Ö.Ç. and N.C.; investigation, Ö.Ç. and N.C.; resources, Ö.Ç. and N.C.; data curation, Ö.Ç. and N.C.; writing—original draft preparation, Ö.Ç.; writing—review and editing, Ö.Ç. and N.C.; visualization, Ö.Ç. and N.C.; supervision, Ö.Ç. and N.C.; project administration, Ö.Ç.; funding acquisition, Ö.Ç. All authors have read and agreed to the published version of the manuscript.

5.2. Data Availability Statement

The data presented in this study are available in the article.

5.3. Funding

The authors received no financial support for the research, authorship, and/or publication of this article.

5.4. Institutional Review Board Statement

Not applicable.

5.5. Informed Consent Statement

Not applicable.

5.6. Declaration of Competing Interest

The authors declare that there is no conflict of interests regarding the publication of this manuscript. In addition, the ethical issues, including plagiarism, informed consent, misconduct, data fabrication and/or falsification, double publication and/or submission, and redundancies have been completely observed by the authors.

6. References

[1] Çakır, Ö. (2020). Transverse Isotropic Crust Structure Beneath the Northwest and Central North Anatolia Revealed By Seismic Surface Waves Propagation. Malaysian Journal of Geosciences, 5(2), 41–50. doi:10.26480/mjg.02.2021.41.50.

[2] Calderón-Macías, C., & Luke, B. (2007). Improved parameterization to invert Rayleigh-wave data for shallow profiles containing stiff inclusions. Geophysics, 72(1), 1– 10. doi:10.1190/1.2374854.

[3] Pasquet, S., Bodet, L., Longuevergne, L., Dhemaied, A., Camerlynck, C., Rejiba, F., & Guérin, R. (2015). 2D characterization of near-surface VP/VS: Surface-wave dispersion inversion versus refraction tomography. Near Surface Geophysics, 13(4), 315–331. doi:10.3997/1873-0604.2015028.

[4] Pasion, L. R., Billings, S. D., & Oldenburg, D. W. (2003). Joint and Cooperative Inversion of Magnetic and Time Domain Electromagnetic Data for the Characterization of UXO. Proceedings from SAGEEP 03, 1455–1468. doi:10.4133/1.2923153.

[5] Piatti, C., Socco, L. V., Boiero, D., & Foti, S. (2013). Constrained 1D joint inversion of seismic surface waves and P-refraction traveltimes. Geophysical Prospecting, 61(SUPPL.1), 77–93. doi:10.1111/j.1365-2478.2012.01071.x.

[6] Ronczka, M., Hellman, K., Günther, T., Wisén, R., & Dahlin, T. (2017). Electric resistivity and seismic refraction tomography: A challenging joint underwater survey at Äspö Hard Rock Laboratory. Solid Earth, 8(3), 671–682. doi:10.5194/se-8-671-2017.

[7] Monteiro Santos, F. A., Sultan, S. A., Represas, P., & El Sorady, A. L. (2006). Joint inversion of gravity and geoelectrical data for groundwater and structural investigation: Application to the northwestern part of Sinai, Egypt. Geophysical Journal International, 165(3), 705–718. doi:10.1111/j.1365-246X.2006.02923.x.

[8] Schwenk, J. T., Sloan, S. D., Ivanov, J., & Miller, R. D. (2016). Surface-wave methods for anomaly detection. Geophysics, 81(4), EN29–EN42. doi:10.1190/GEO2015-0356.1.

[9] Zhang, Z. dong, Saygin, E., He, L., & Alkhalifah, T. (2021). Rayleigh Wave Dispersion Spectrum Inversion Across Scales. Surveys in Geophysics, 42(6), 1281–1303. doi:10.1007/s10712-021-09667-z.

[10] Li, G. F., Zheng, H., Zhu, W. L., Wang, M. C., & Zhai, T. L. (2016). Tomographic inversion of near-surface Q factor by combining surface and cross-hole seismic surveys. Applied Geophysics, 13(1), 93–102. doi:10.1007/s11770-016-0544-2.

[11] Çaklr, Ö. (2019). Love and Rayleigh waves inverted for vertical transverse isotropic crust structure beneath the Biga Peninsula and the surrounding area in NW Turkey. Geophysical Journal International, 216(3), 2081–2105. doi:10.1093/gji/ggy538.

[12] Hosseini, K., Sigloch, K., Tsekhmistrenko, M., Zaheri, A., Nissen-Meyer, T., & Igel, H. (2020). Global mantle structure from multifrequency tomography using P, PP and P-diffracted waves. Geophysical Journal International, 220(1), 96–141. doi:10.1093/gji/ggz394.

[13] Abdel Zaher, M., Saibi, H., Mansour, K., Khalil, A., & Soliman, M. (2018). Geothermal exploration using airborne gravity and magnetic data at Siwa Oasis, Western Desert, Egypt. Renewable and Sustainable Energy Reviews, 82, 3824–3832. doi:10.1016/j.rser.2017.10.088.

[14] Çakır, Ö., & Coşkun, N. (2021). Theoretical Issues with Rayleigh Surface Waves and Geoelectrical Method Used for the Inversion of Near Surface Geophysical Structure. Journal of Human, Earth, and Future, 2(3), 183–199. doi:10.28991/hef-2021-02-03-01.

[15] Arzate, J., Corbo-Camargo, F., Carrasco-Núñez, G., Hernández, J., & Yutsis, V. (2018). The Los Humeros (Mexico) geothermal field model deduced from new geophysical and geological data. Geothermics, 71, 200–211. doi:10.1016/j.geothermics.2017.09.009.

[16] Horrocks, T., Holden, E. J., Wedge, D., & Wijns, C. (2021). 3-D geochemical interpolation guided by geophysical inversion models. Geoscience Frontiers, 12(3), 101089. doi:10.1016/j.gsf.2020.09.018.

[17] Huang, T., Fu, X., Ge, L., Zou, F., Hao, X., Yang, R., Xiao, R., & Fan, J. (2020). The genesis of giant lithium pegmatite veins in Jiajika, Sichuan, China: Insights from geophysical, geochemical as well as structural geology approach. Ore Geology Reviews, 124, 103557. doi:10.1016/j.oregeorev.2020.103557.

[18] Martinho, E., & Dionísio, A. (2014). Main geophysical techniques used for non-destructive evaluation in cultural built heritage: A review. Journal of Geophysics and Engineering, 11(5), 53001. doi:10.1088/1742-2132/11/5/053001.

[19] Çakır, Ö., & Erduran, M. (2011). On the P and S Receiver Functions Used for Inverting the One-Dimensional Upper Mantle Shear-Wave Velocities. Surveys in Geophysics, 32(1), 71–98. doi:10.1007/s10712-010-9108-9.

[20] Fishwick, S. (2010). Surface wave tomography: Imaging of the lithosphere-asthenosphere boundary beneath central and southern Africa? Lithos, 120(1–2), 63–73. doi:10.1016/j.lithos.2010.05.011.

[21] Lu, Y., Stehly, L., & Paul, A. (2018). High-resolution surface wave tomography of the European crust and uppermost mantle from ambient seismic noise. Geophysical Journal International, 214(2), 1136–1150. doi:10.1093/gji/ggy188.

[22] Pan, Y., Schaneng, S., Steinweg, T., & Bohlen, T. (2018). Estimating S-wave velocities from 3D 9-component shallow seismic data using local Rayleigh-wave dispersion curves – A field study. Journal of Applied Geophysics, 159, 532–539. doi:10.1016/j.jappgeo.2018.09.037.

[23] D. W. Steeples. (2009). A review of shallow seismic methods. Annals of Geophysics, 43(6), 1021–1044. doi:10.4401/ag-3687.

[24] Yuan, X., Kind, R., Li, X., & Wang, R. (2006). The S receiver functions: Synthetics and data example. Geophysical Journal International, 165(2), 555–564. doi:10.1111/j.1365-246X.2006.02885.x.

[25] Dal Moro, G., & Pipan, M. (2007). Joint inversion of surface wave dispersion curves and reflection travel times via multi-objective evolutionary algorithms. Journal of Applied Geophysics, 61(1), 56–81. doi:10.1016/j.jappgeo.2006.04.001.

[26] Vinnik, L. P., Erduran, M., Oreshin, S. I., Kosarev, G. L., Kutlu, Y. A., Çakir, Ö., & Kiselev, S. G. (2014). Joint inversion of P- and S-receiver functions and dispersion curves of Rayleigh waves: The results for the Central Anatolian Plateau. Izvestiya, Physics of the Solid Earth, 50(5), 622–631. doi:10.1134/S106935131404017X.

[27] Chen, Y., & Niu, F. (2016). Joint inversion of receiver functions and surface waves with enhanced preconditioning on densely distributed CNDSN stations: Crustal and upper mantle structure beneath China. Journal of Geophysical Research: Solid Earth, 121(2), 743–766. doi:10.1002/2015JB012450.

[28] Yin, X., Xu, H., Mi, B., Hao, X., Wang, P., & Zhang, K. (2020). Joint inversion of Rayleigh and Love wave dispersion curves for improving the accuracy of near-surface S-wave velocities. Journal of Applied Geophysics, 176, 103939. doi:10.1016/j.jappgeo.2019.103939.

[29] Onyebueke, E. O., Manzi, M. S. D., & Durrheim, R. J. (2018). High-resolution shallow reflection seismic integrated with other geophysical methods for hydrogeological prospecting in the Nylsvley Nature Reserve, South Africa. Journal of Geophysics and Engineering, 15(6), 2658–2673. doi:10.1088/1742-2140/aadbe3.

[30] Senkaya, M., Karsli, H., Socco, L. V., & Foti, S. (2020). Obtaining reliable S-wave velocity depth profile by joint inversion of geophysical data: the combination of active surface-wave, seismic refraction and electric sounding data. Near Surface Geophysics, 18(6), 659–682. doi:10.1002/nsg.12126.

[31] Filina, I., Liu, M., & Beutel, E. (2020). Evidence of ridge propagation in the eastern Gulf of Mexico from integrated analysis of potential fields and seismic data. Tectonophysics, 775, 228307. doi:10.1016/j.tecto.2019.228307.

[32] C.C. Uwaezuoke, K.S. Ishola, & E. A. Ayolabi. (2021). Electrical resistivity imaging and multichannel analysis of surface waves for mapping the subsurface of a Wetland Area of Lagos, Nigeria. NRIAG Journal of Astronomy and Geophysics, 10(1), 300–319. doi:10.1080/20909977.2021.1927427.

[33] Martínez-Moreno, F. J., Galindo-Zaldívar, J., Pedrera, A., Teixido, T., Ruano, P., Peña, J. A., González-Castillo, L., Ruiz-Constán, A., López-Chicano, M., & Martín-Rosales, W. (2014). Integrated geophysical methods for studying the karst system of Gruta de las Maravillas (Aracena, Southwest Spain). Journal of Applied Geophysics, 107, 149–162. doi:10.1016/j.jappgeo.2014.05.021.

[34] Moorkamp, M. (2017). Integrating Electromagnetic Data with Other Geophysical Observations for Enhanced Imaging of the Earth: A Tutorial and Review. Surveys in Geophysics, 38(5), 935–962. doi:10.1007/s10712-017-9413-7.

[35] Parsekian, A. D., Singha, K., Minsley, B. J., Holbrook, W. S., & Slater, L. (2015). Multiscale geophysical imaging of the critical zone. Reviews of Geophysics, 53(1), 1–26. doi:10.1002/2014RG000465.

[36] Levshin, A. L., Barmin, M. P., & Ritzwoller, M. H. (2018). Tutorial review of seismic surface waves' phenomenology. Journal of Seismology, 22(2), 519–537. doi:10.1007/s10950-017-9716-7.

[37] Luo, Y., Xia, J., Xu, Y., & Zeng, C. (2011). Analysis of group-velocity dispersion of high-frequency Rayleigh waves for near-surface applications. Journal of Applied Geophysics, 74(2–3), 157–165. doi:10.1016/j.jappgeo.2011.04.002.

[38] Bharti, A. K., Prakash, A., Verma, A., & Singh, K. K. K. (2021). Assessment of hydrological condition in strata associated with old mine working during and post-monsoon using electrical resistivity tomography: a case study. Bulletin of Engineering Geology and the Environment, 80(6), 5159–5166. doi:10.1007/s10064-021-02208-3.

[39] Coşkun, N., Çakır, Ö., Erduran, M., Kutlu, Y. A., & Yalçın, A. (2016). Preliminary investigation of underground settlements of Nevşehir Castle region using 2.5-D electrical resistivity tomography: Cappadocia, Turkey. Arabian Journal of Geosciences, 9(18), 717. doi:10.1007/s12517-016-2727-9.

[40] Coşkun, N., Çakır, Ö., Erduran, M., Kutlu, Y. A., & Çetiner, Z. S. (2016). A potential landslide area investigated by 2.5D electrical resistivity tomography: case study from Çanakkale, Turkey. Arabian Journal of Geosciences, 9(1), 1–20. doi:10.1007/s12517-015-2026-x.

[41] Das, P., Pal, S. K., Mohanty, P. R., Priyam, P., Bharti, A. K., & Kumar, R. (2017). Abandoned mine galleries detection using electrical resistivity tomography method over Jharia coal field, India. Journal of the Geological Society of India, 90(2), 169–174. doi:10.1007/s12594-017-0695-7.

[42] Srivastava, S., Pal, S. K., & Kumar, R. (2020). A time-lapse study using self-potential and electrical resistivity tomography methods for mapping of old mine working across railway-tracks in a part of Raniganj coalfield, India. Environmental Earth Sciences, 79(13), 332. doi:10.1007/s12665-020-09067-3.

[43] Coşkun, N. (1994). A comparison of configuration arrays for the resistivity and induced polarisation methods and a direct interpretation technique for vertical profiling field data, PhD Dissertation, University of York, York, United Kingdom.

[44] Çakir, Ö. (2006). The multilevel fast multipole method for forward modelling the multiply scattered seismic surface waves. Geophysical Journal International, 167(2), 663–678. doi:10.1111/j.1365-246X.2006.02928.x.

[45] Çakir, Ö. (2012). A multilevel fast multipole method for computing the propagation of multiply scattered 2.5-D teleseismic surface waves underneath a linear or quasi-linear seismic station array. International Journal of Physical Sciences, 7(42), 5687–5700. doi:10.5897/IJPS12.337.

[46] Filippi, C., Leparoux, D., Grandjean, G., Bitri, A., & Côte, P. (2019). New robust observables on Rayleigh waves affected by an underground cavity: From numerical to experimental modelling. Geophysical Journal International, 218(3), 1903–1918. doi:10.1093/gji/ggz256.

[47] Lu, L., Maupin, V., Zeng, R., & Ding, Z. (2008). Scattering of surface waves modelled by the integral equation method. Geophysical Journal International, 174(3), 857–872. doi:10.1111/j.1365-246X.2008.03787.x.

[48] Nasseri-Moghaddam, A. (2006). Study of the effect of lateral inhomogeneities on the propagation of Rayleigh waves in an elastic medium, PhD Dissertation, University of Waterloo, Waterloo, Canada.

[49] Shao, G., Tsoflias, G. P., & Li, C. (2016). Detection of near-surface cavities by generalized S-transform of Rayleigh waves. Journal of Applied Geophysics, 129, 53–65. doi:10.1016/j.jappgeo.2016.03.041.

[50] Xia, J., Nyquist, J. E., Xu, Y., Roth, M. J. S., & Miller, R. D. (2007). Feasibility of detecting near-surface feature with Rayleigh-wave diffraction. Journal of Applied Geophysics, 62(3), 244–253. doi:10.1016/j.jappgeo.2006.12.002.

[51] Xu, C.Q. (2010). Localization of Near-Surface Anomalies Using Seismic Rayleigh Waves, PhD Dissertation, Dalhousie University, Halifax, Canada.

[52] Breithaupt, C. (2016). Cave detection using seismic methods at Madison Blue Spring State Park, Madison County, Florida, MSc Thesis, Michigan Technological University, Houghton, United States.

[53] Rahnema, H., Mirassi, S., & Dal Moro, G. (2021). Cavity effect on Rayleigh wave dispersion and P-wave refraction. Earthquake Engineering and Engineering Vibration, 20(1), 79–88. doi:10.1007/s11803-021-2006-y.

[54] Barone, I., Boaga, J., Carrera, A., Flores-Orozco, A., & Cassiani, G. (2021). Tackling Lateral Variability Using Surface Waves: A Tomography-Like Approach. Surveys in Geophysics, 42(2), 317–338. doi:10.1007/s10712-021-09631-x.

[55] Herrmann, R.B. (2002). Computer programs in seismology, version 3.30. St. Louis University, Missouri, United States.

[56] Blanchy, G., Saneiyan, S., Boyd, J., McLachlan, P., & Binley, A. (2020). ResIPy, an intuitive open source software for complex geoelectrical inversion/modeling. Computers and Geosciences, 137, 104423. doi:10.1016/j.cageo.2020.104423.

[57] Aki, K., Richards, P.G., (1980). Quantitative Seismology: Theory and Methods, pp. 144–151 & 315–319, W. H. Freeman, San Francisco, CA, United States.

[58] Dziewonski, A., Bloch, S., & Landisman, M. (1969). A technique for the analysis of transient seismic signals. Bulletin of the Seismological Society of America, 59(1), 427–444. doi:10.1785/bssa0590010427.

[59] Cakir, O. (1989). High frequency Rayleigh and Love waves, MS Thesis, Texas Tech University, Lubbock Texas, United States.

[60] Cakir, O. (1993). Propagation of high frequency P and S waves under oceanic structures, PhD Dissertation, Texas Tech University, Lubbock Texas, United States.

[61] Ismet Kanli, A., Tildy, P., Prónay, Z., Pinar, A., & Hermann, L. (2006). Vs30 mapping and soil classification for seismic site effect evaluation in Dinar region, SW Turkey. Geophysical Journal International, 165(1), 223–235. doi:10.1111/j.1365-246X.2006.02882.x.

[62] Keceli, A. (2012). Soil parameters which can be determined with seismic velocities. Jeofizik 16: 17–29.

[63] Milsom, J. (2003). Field Geophysics, the Geological Field Guide Series, Third Edition, Willey, England.

[64] Palacky, G. J. (1988). 3. Resistivity Characteristics of Geologic Targets. Electromagnetic Methods in Applied Geophysics, 1, 52–129. doi:10.1190/1.9781560802631.ch3.